

TransCL: Transformer Makes Strong and Flexible Compressive Learning

Chong Mou, Jian Zhang

Abstract—Compressive learning (CL) is an emerging framework that integrates signal acquisition via compressed sensing (CS) and machine learning for inference tasks directly on a small number of measurements. It can be a promising alternative to classical image-domain methods and enjoys great advantages in memory saving and computational efficiency. However, previous attempts on CL are not only limited to a fixed CS ratio, which lacks flexibility, but also limited to MNIST/CIFAR-like datasets and do not scale to complex real-world high-resolution (HR) data or vision tasks. In this paper, a novel transformer-based compressive learning framework on large-scale images with arbitrary CS ratios, dubbed TransCL, is proposed. Specifically, TransCL first utilizes the strategy of learnable block-based compressed sensing and proposes a flexible linear projection strategy to enable CL to be performed on large-scale images in an efficient block-by-block manner with arbitrary CS ratios. Then, regarding CS measurements from all blocks as a sequence, a pure transformer-based backbone is deployed to perform vision tasks with various task-oriented heads. Our sufficient analysis presents that TransCL exhibits strong resistance to interference and robust adaptability to arbitrary CS ratios. Extensive experiments for complex HR data demonstrate that the proposed TransCL can achieve state-of-the-art performance in image classification and semantic segmentation tasks. In particular, TransCL with a CS ratio of 10% can obtain almost the same performance as when operating directly on the original data and can still obtain satisfying performance even with an extremely low CS ratio of 1%. The source codes of our proposed TransCL is available at <https://github.com/MC-E/TransCL>.

Index Terms—Compressed sensing, Compressive learning, Transformer, Image classification, Semantic segmentation.

1 INTRODUCTION

SIGNAL acquisition and processing methods have changed substantially over the last several decades. Many methods have moved from the analog to the digital domain, creating sensing systems that are more robust, flexible, and cost-effective than their analog counterparts. However, in many important real-world applications, the resulting Nyquist rate is so high that it is not viable or even physically impossible. Compressed sensing (CS), built upon the groundbreaking works by Candes *et al.* [1] and Donoho *et al.* [2], has become a more efficient and hardware-friendly signal acquisition method and has been receiving more and more attention. CS theory shows that when a signal has a sparse representation on a certain basis, one can vastly reduce the number of required samples—below the Nyquist rate and can still recover the signal perfectly from its CS measurement. CS has been applied in many practical applications, including but not limited to single-pixel imaging [3], [4], accelerating magnetic resonance imaging (MRI) [5], wireless telemonitoring [6], cognitive radio communication [7], and snap compressive imaging [8], [9]. Correspondingly, there exist several types of CS equipments, *e.g.*, single-pixel camera [3], flexible voxels camera [10], and P2C2 camera [11], which can project images from the high-dimensional image domain to the low-dimensional measurement domain.

Most of the recent works [12], [13], [14], [15], [16], [17], [18], [19] in the CS community focus on how to reconstruct

the original signal, and less attention has been devoted to whether one can perform high-level vision tasks direct in the measurement domain. However, in many applications, such as classification and segmentation, we are not interested in obtaining a precise reconstruction of the scene under view, but rather are only interested in the results of inference tasks. There also exist coupling problems between the reconstruction results and the inference model trained on natural images. Moreover, with the development of deep learning, data privacy has gradually become a concern [20], [21]. Thus, in some specific applications, signal reconstruction is undesirable since this step can potentially disclose private information. Directly performing inference tasks in the measurement domain without knowing the sampling matrix makes it almost inaccessible to original visual perception, which is an appropriate scheme to protect data privacy during network training and inference.

Calderbank *et al.* [22] and Davenport *et al.* [23] first construct the concept of compressive learning (CL) in which the inference system is directly built on the top of CS measurements without an explicit reconstruction step. Some theoretical demonstrations of CL have been made in [24], [25]. Some early works have been made in [26], [27], [28], [29]. The very recent researches (Tran *et al.* [30], [31]) propose an efficient method to exploit the multidimensional property of CL. Although there have been several novel attempts, some intractable problems make existing compressive learning methods not yet comparable to the image-domain methods. **First**, the information loss during the CS sampling process due to the lax sparsity of natural images makes the performance of CL significantly lower than image-domain methods. **Second**, a large-scale sampling matrix and large matrix multiplication are needed to project real-world images, making the sampling process complicated. The high complexity in CS of high-resolution images is the reason of

- C. Mou and J. Zhang are with the School of Electronic and Computer Engineering, Peking University Shenzhen Graduate School, Shenzhen 518055, China. Jian Zhang is also with the Peng Cheng Laboratory, Shenzhen, China. (Corresponding author: Jian Zhang.)
E-mail: eechongm@stu.pku.edu.cn; zhangjian.sz@pku.edu.cn

Manuscript received August 26, 2021; revised December 10, 2021, March 24, 2022 and July 6, 2022; accepted July 14, 2022. This work was supported by National Natural Science Foundation of China (61902009).

limiting existing CL methods [26], [27], [28], [29], [30], [31] to MNIST/CIFAR-like datasets [32], [33]. **Third**, different CS ratios will generate measurement vectors with different lengths, leading to the fact that most CL methods can only perform inference tasks with a fixed CS ratio, limiting their practice in some real-world applications. In this paper, we propose several solutions to solve these weaknesses, helping bridge the gap between CL and image-domain methods.

In fact, an image and its CS measurement have a lot in common, and several helpful priors in the image domain can also be applied in the measurement domain. For instance, the non-local self-similarity prior, which assumes that similar content would recur across the whole scene. This prior has been widely used in the community of image reconstruction [34], [35]. However, how to combine this effective prior naturally into CL to resist the information loss has been hardly studied. Recently, Transformer (Vaswani *et al.* [36]) has attracted more and more attention from the community of computer vision. This family of networks [36], [37], [38], [39], *i.e.*, transformer networks, originate from machine translation and require serialized inputs, and are very good at modeling long-range correlations in sequences. Thus, transformer can be applied in CL to compensate for information loss through element-wise correlations. In order to make complex real-world data tractable, we propose to adopt the strategy of block-based compressed sensing (BCS) [40], [41] into CL, which applies CS to image blocks through the same operator to generate a sequence of CS measurements instead of an entire one. BCS is mostly suitable for processing very large-scale images in CL, while requiring significantly less memory to store the sensing matrix and provides a serialized input to the transformer layer. Thus, a significant finding is that BCS and Transformer can be well combined to solve the two main challenges faced by existing CL methods, which greatly inspires our proposed TransCL framework. We further propose a flexible linear projection to enable a single model to handle input measurements with arbitrary CS ratios. In addition, our TransCL exploits a learnable binary sampling matrix, which is more practical and hardware-friendly.

The main contributions of this paper are summarized as follows:

- We reformulate the CL problem from a sequence-to-sequence sensing and learning perspective and propose a novel transformer-based CL framework, dubbed TransCL. Our TransCL can be generalized to more complex high-level vision tasks and real-world benchmarks, which helps bridge the gap between inference tasks in the image and measurement domains.
- We propose a flexible projection scheme to enable a single model to sample and infer images with arbitrary CS ratios. In this way, our method can be trained only once to deal with general cases.
- We propose incorporating the strategy of learnable block-based compressed sensing (BCS) and binary sampling matrix into CL, making the whole system more memory-saving and hardware-friendly.
- Extensive experiments demonstrate that our TransCL can achieve state-of-the-art performance in various compressive learning tasks (*i.e.*, image classification and semantic segmentation), especially at extremely

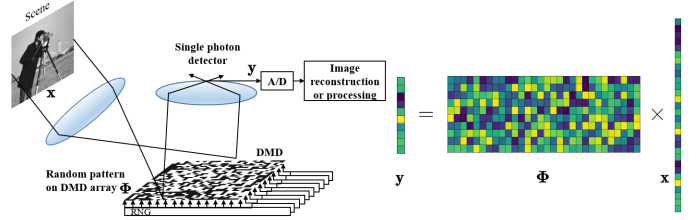


Fig. 1. Illustration of CS acquisition for a still image with a single-pixel camera [2], which can be formulated as $y = \Phi x$.

low CS ratios (*e.g.*, 1%). We further verify the robustness of our TransCL in the face of disturbances.

2 RELATED WORK

Our proposed TransCL is closely related to existing compressed sensing methods, compressive learning methods, and transformer networks. Thus, in what follows, we give a brief review of these aspects and focus on the specific methods most relevant to our own.

2.1 Compressed Sensing

Compressed sensing (CS) [2] is an emerging mathematical paradigm that permits, under certain conditions, linear projection of a signal into a dimension much lower than that of the original signal while allowing exact recovery of the signal from its projection. That is, from much fewer acquired measurements than determined by Nyquist sampling theory, CS theory demonstrates that a signal can be reconstructed with high probability when it exhibits sparsity in some transform domain. This novel acquisition strategy is much more hardware-friendly and enables image or video acquisition with a sub-Nyquist sampling rate. By leveraging the redundancy inherent to a signal, CS conducts sampling and compression at the same time, which greatly alleviates the need for high transmission bandwidth and large storage space, enabling low-cost on-sensor data compression.

Concretely, suppose we have the CS measurement $y \in \mathbb{R}^M$ of the signal $x \in \mathbb{R}^N$, *i.e.*, $y = \Phi x$, where $M \ll N$, $\Phi \in \mathbb{R}^{M \times N}$ is the sampling matrix, and CS ratio is defined as $\gamma = \frac{M}{N}$. Because the number of unknowns is much larger than the number of observations, reconstructing x from its corresponding y is impossible in general; however, if x is known to be sufficiently sparse in some domain, the exact recovery of x is possible—that is the fundamental tenet of CS theory. Fig. 1 illustrates the CS acquisition process of a still image with a single-pixel camera.

Since the advent of the CS, most methods [12], [13], [14], [15] focus on the inverse problem of CS, which aims to fully recover the signal from its CS measurement. Given the linear measurement y , traditional reconstruction methods usually restore the original signal by solving the following optimization problem:

$$\min_x \frac{1}{2} \|\Phi x - y\|_2^2 + \lambda \|\psi(x)\|_1, \quad (1)$$

where $\psi(x)$ represents the transformation of x with respect to some transform operator $\psi(\cdot)$, and the sparsity of $\psi(x)$ is encouraged by the ℓ_1 norm with λ being the regularization parameter (generally pre-defined). However, in many high-level applications, we are not interested in obtaining a

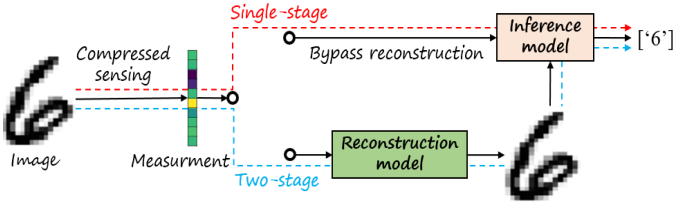


Fig. 2. Illustration of two ways of performing inference tasks (i.e., image classification) on CS measurements. The blue dashed line presents the conventional two-stage operation (reconstruction first and then inference in the image domain), and the red dashed line represents the single-stage compressive learning (CL) direct in the measurement domain.

precise reconstruction of the scene under view, but rather are the results of specific inference tasks.

2.2 Compressive Learning

As illustrated by the red dashed line in Fig. 2, compressive learning (CL) aims to directly perform inference tasks in the measurement domain without signal reconstruction. The concept of CL is first constructed in [22], [23]. This strategy bypasses the reconstruction process and greatly reduces the amount of data. Thus, it is highly cost-effective in terms of storage memory and computational complexity. Moreover, it can help to protect data privacy. The theoretical basics of CL have been well established. The early research [22] demonstrates that given certain conditions of the sampling matrix Φ , the performance of a linear support vector machine (SVM) trained on CS measurements is as good as the best linear threshold classifier trained on the original signal. [24] proves that the Kullback-Leibler and Chernoff distances between two probability density functions are preserved up to a factor of $\frac{M}{N}$, where M and N represent the length of the CS measurement and original signal, respectively. [25] exploits the performance bound under perturbation bringing from the uncertainty of the measurement matrix. Some early works [26], [27], [28], [29] study directly performing inference tasks in the measurement domain. [42] applies CL to action recognition. With the advances in computing hardware and stochastic optimization techniques, [43], [44] propose to jointly optimize the sampling matrix with the whole network in an end-to-end manner. Benefiting from the programmable CS methods [45], [46], the learned sampling matrix has the opportunity to be deployed to hardware for CS. The very recent researches [30], [31] propose an efficient method to exploit the multidimensional property of CL. However, existing CL methods are restricted to a small range of high-level vision tasks (e.g., image classification/recognition). These methods are usually difficult or unstable [47] to handle large-scale images, and most works focus on small datasets, such as MNIST [32] and CIFAR [33], not comparable to complex real-world high-resolution data. Furthermore, these CL methods only handle inference tasks with a fixed CS ratio without considering the variation of CS ratio in practical applications.

2.3 Transformer

Transformer was first introduced in [36] for machine translation, which is a self-attention mechanism to construct long-range correlations for elements in different places. Given an input sequence $\mathbf{E} \in \mathbb{R}^{C \times L}$ with the sequence length being

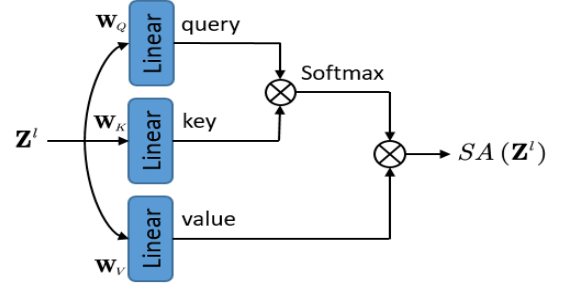


Fig. 3. Illustration of the self-attention (SA) mechanism [36], which is used to construct long-range correlations among the input sequence.

L and the number of channels being C , a pure transformer layer has a global receptive field to build correlations for information transfer. At the beginning of the transformer network, each element of the input sequence is first embedded by a linear projection $\mathbf{W} \in \mathbb{R}^{d \times C}$ to the length of d and then added by the position embedding $\mathbf{P} \in \mathbb{R}^{d \times L}$. Let $\mathbf{Z}^l \in \mathbb{R}^{d \times L}$ represent the input of the l -th transformer layer. The core component is a self-attention module with multiple heads. As illustrated in Fig. 3, each head performs non-local operation in a triplet of embedded features (*query*, *key*, *value*) computed from the input as:

$$\text{query} = \mathbf{W}_Q \mathbf{Z}^l, \text{key} = \mathbf{W}_K \mathbf{Z}^l, \text{value} = \mathbf{W}_V \mathbf{Z}^l, \quad (2)$$

where $\mathbf{W}_Q, \mathbf{W}_K, \mathbf{W}_V \in \mathbb{R}^{d \times d}$ are the learnable parameters of three linear projection layers. The self-attention operation can be formally defined as:

$$\text{SA}(\mathbf{Z}^l) = (\mathbf{W}_V \mathbf{Z}^l) \text{Softmax} \left(\frac{(\mathbf{W}_Q \mathbf{Z}^l)^\top \mathbf{W}_K \mathbf{Z}^l}{\sqrt{d}} \right). \quad (3)$$

However, there exists a gap between $2D$ image and $1D$ sequence in applying transformer to vision tasks. A straightforward method [48] is to flat an input feature map $\mathbf{F}_{in} \in \mathbb{R}^{C \times H \times W}$ into a sequence with the length of HW . Given the quadratic model complexity of the transformer, it is not possible to handle the input sequence with high dimensions. [49] proposed a solution to unfold an input image into a sequence of image blocks with each block size being $B \times B$, significantly reducing the sequence length to $\frac{HW}{B^2}$. This strategy can reduce the computational complexity of the transformer layer. Since ViT was proposed [49], there have been several attempts to adapt transformers towards vision tasks, including image classification [50], [51], object detection [52], [53], segmentation [54], human pose estimation [55], and image restoration [56], [57], [58]. However, this strategy has hardly been studied in the community of compressive learning (CL) and compressed sensing (CS).

3 METHODOLOGY

In this section, we will elaborate on our proposed strong and flexible transformer-based compressive learning framework, dubbed TransCL.

3.1 Framework

The global architecture of our TransCL is presented in Fig. 4, which is mainly composed of a Compressed Sensing Module (CSM), a Transformer-based Backbone (TB), and a

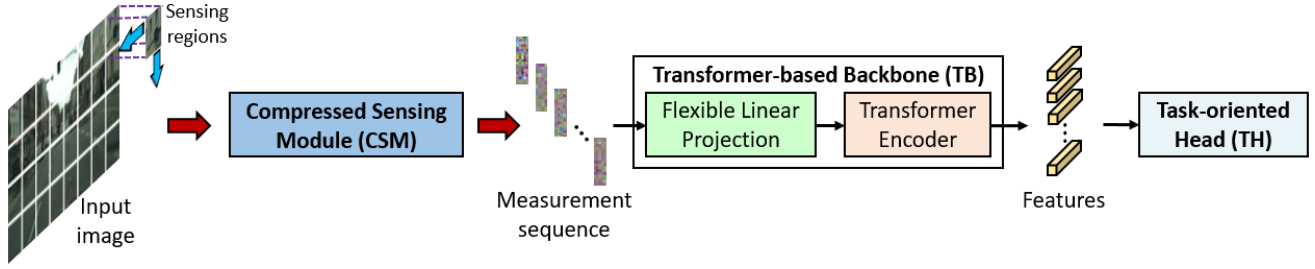


Fig. 4. An overview of our proposed transformer-based compressive learning (TransCL) framework, which is composed of compressed sensing module (CSM), Transformer-based Backbone (TB) and Task-oriented Head (TH).

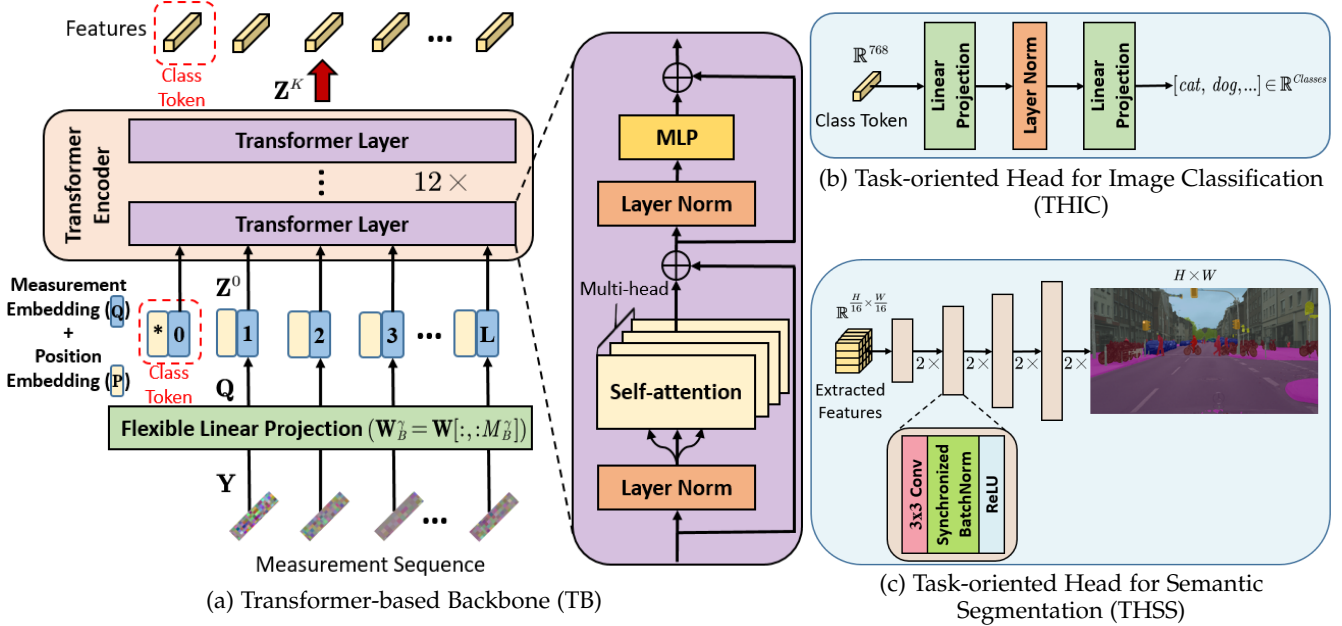


Fig. 5. Detailed architectures of transformer-based backbone (TB) and task-oriented heads (TH) in our TransCL. (a) presents the details of our transformer-based backbone (TB). (b) is the illustration of task-oriented head for image classification (THIC). (c) presents the details of task-oriented head for semantic segmentation (THSS), which is a plain network to perform upsampling and predicting in a progressive manner.

Task-oriented Head (TH). Note that our TransCL targets performing high-level vision tasks on real-world images, rectifying the information loss in the measurement domain and handling input with arbitrary CS ratios. CSM is designed to perform sensing and compressing in a block-by-block manner with arbitrary CS ratios, and it is jointly optimized with the whole network. To handle the serialized output of CSM and resist information loss, TB is designed as a pure transformer architecture. A creative modulation is that TB begins with a flexible linear projection (FLP) layer to project the input with arbitrary CS ratios to a set of measurement embeddings with the same vector length. Based on TB, Th utilizes the extracted features to perform specific vision tasks. We will provide the details below.

3.2 Compressed Sensing Module

As illustrated in Fig. 4, CSM is a data acquisition step via CS, aiming to compress the scene to a small number of measurements through a linear sampling matrix Φ . In our TransCL, we set Φ as a trainable parameter, which is jointly optimized with the whole network. Based on these basic settings, we carry out more elaborate designs to make CSM powerful and flexible.

3.2.1 Efficient Block-based Arbitrary Sampling

Due to the high computational complexity in sampling large-scale images, most existing CL methods are limited in MNIST/CIFAR-like datasets. To process high-resolution images in real-world applications and provide serialized measurements to the transformer-based backbone (TB), we propose to apply the strategy of block-based compressed sensing (BCS) [40] [41] to CL tasks. BCS is able to sense and compress images in a block-by-block manner through the same operator, which has the advantage of decreasing the bandwidth required to transmit measurement vectors between system memory and the DMD array. Specifically, given a high-resolution input image of size $H \times W$. Instead of direct CS by a large sampling matrix $\Phi \in \mathbb{R}^{M \times N}$, where $M = \gamma N$ and $N = HW$. As shown in Fig. 6, we first divide the image into L non-overlapped blocks with each block size being $B \times B$ and $L = \frac{HW}{B^2}$. Denote $\mathbf{x}_i \in \mathbb{R}^{B^2}$ as the vectorized representation of the i -th image block and define $\mathbf{X} = [\mathbf{x}_1, \mathbf{x}_2, \dots, \mathbf{x}_L]$. The corresponding block-based sampling matrix is represented as $\Phi_B^\gamma \in \mathbb{R}^{M_B^\gamma \times B^2}$, where $M_B^\gamma = \gamma B^2$. Then, the resulting CS measurement $\mathbf{y}_i \in \mathbb{R}^{M_B^\gamma}$ is generated by $\mathbf{y}_i = \Phi_B^\gamma \mathbf{x}_i$. Finally, our CSM generates a sequence of measurements: $\mathbf{Y} = [\mathbf{y}_1, \mathbf{y}_2, \dots, \mathbf{y}_L]$. The output

of CSM is formulated as:

$$\mathbf{Y} = \Phi_B^\gamma \mathbf{X}, \quad (4)$$

where $\mathbf{Y} \in \mathbb{R}^{M_B^\gamma \times L}$. Note that BCS only needs to store a block-based sampling matrix instead of a full one and greatly reduces the computational burden of matrix multiplication through a block-by-block strategy, which is quite memory efficient. In addition, BCS can also be easily implemented on hardware by introducing a mask for each square region to drive the DMD of the single-pixel camera to route light from each region to the detector one by one [59] [60].

Furthermore, unlike existing methods [30], [31], [43], [44], [61] for jointly optimizing the sampling matrix and inference model for a fixed CS ratio each time, we propose a learnable and powerful CSM, which can generate a block-based sampling matrix with arbitrary CS ratio γ by training once. Our proposed sampling scheme is presented in Fig. 7(a). As a reusable scheme, we first define a learnable sampling base matrix (SBM) as Φ of size $B^2 \times B^2$. Then, the sampling matrix Φ_B^γ with any CS ratio γ used in Eq. (4) can be directly constructed by truncating the first M_B^γ rows from SBM Φ , i.e., $\Phi_B^\gamma = \Phi[:M_B^\gamma]$. Hence, our CSM only needs one learnable SBM to generate matrices with arbitrary sampling ratios (B^2 in total), and it only needs to be trained once, without introducing B^2 different sampling matrices as learnable parameters and training for B^2 times.

3.2.2 Hardware-friendly Binary Sampling Design

Although float-point CS matrices have been widely used, the most efficient and energy-saving hardware utilizes binary sampling matrix (1 or -1) in real-world applications. This hardware-friendly choice has been studied in the recent reconstruction work [61]. In this paper, we exploit this property in the field of CL to further train a binary SBM Φ in our CSM. We denote $\tilde{\Phi}$ as the binary version of the float-point SBM Φ , which is computed by $\tilde{\Phi} = \mathcal{B}(\Phi)$, where $\mathcal{B}(\cdot)$ is an element-wise operation defined as:

$$\mathcal{B}(a) = \begin{cases} 1, & \text{if } a \geq 0; \\ -1, & \text{if } a < 0. \end{cases} \quad (5)$$

However, such a setting makes it difficult to calculate the gradient. Inspired by Binarized neural networks (BNN) [62] and differentiable quantization [63], we introduce a proxy function $\tilde{\mathcal{B}}(\cdot)$ to approximate $\mathcal{B}(\cdot)$, which is defined as:

$$\tilde{\mathcal{B}}(a) = \begin{cases} 1, & \text{if } a > 1; \\ a, & \text{if } -1 \leq a \leq 1; \\ -1, & \text{if } a < -1. \end{cases} \quad (6)$$

Thus, the gradient of $\mathcal{B}(\cdot)$, denoted by $\mathcal{B}'(\cdot)$, can be approximated by the gradient of $\tilde{\mathcal{B}}(\cdot)$, denoted by $\tilde{\mathcal{B}}'(\cdot)$, that is:

$$\tilde{\mathcal{B}}'(a) = \begin{cases} 1, & \text{if } -1 \leq a \leq 1; \\ 0, & \text{otherwise.} \end{cases} \quad (7)$$

Therefore, $\mathcal{B}(\cdot)$ is used in the forward propagation, while $\tilde{\mathcal{B}}(\cdot)$ is used in back-propagation.

3.3 Transformer-based Backbone

Fig. 5(a) presents the detailed architecture of our proposed transformer-based backbone (TB), which is used to extract informative features from the serialized measurements \mathbf{Y} with arbitrary CS ratios. TB is composed of a flexible linear

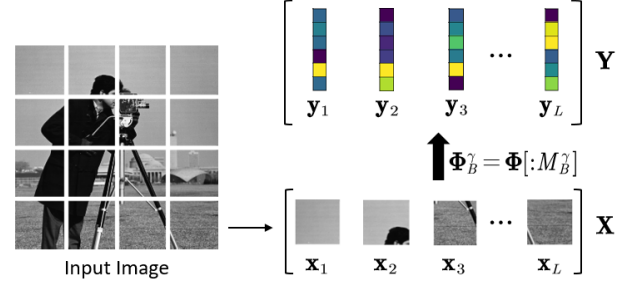


Fig. 6. Illustration of compressed sensing module (CSM) in our TransCL.

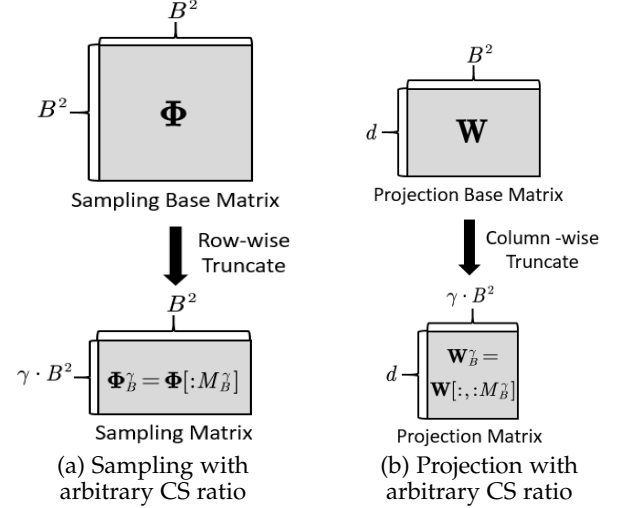


Fig. 7. Illustration of generating the sampling matrix Φ_B^γ and the projection matrix \mathbf{W}_B^γ with arbitrary CS ratio γ from their corresponding base matrices Φ and \mathbf{W} , respectively.

projection (FLP) and a stack of transformer layers [36] dubbed transformer encoder (TE).

Flexible Linear Projection. As shown in Fig. 5(a), our FLP is to project the input measurements \mathbf{Y} of size $M_B^\gamma \times L$ to the measurement embedding \mathbf{Q} of size $d \times L$, followed by adding a set of learnable position embedding, denoted by \mathbf{P} of size $d \times L$. Note that different sampling matrix Φ_B^γ with different γ will produce different \mathbf{Y} with different sizes. To overcome the weakness of existing fixed linear projections that can not handle the measurement vectors with variable lengths and analogous to SBM, we similarly define a trainable projection base matrix (PBM) as \mathbf{W} of size $d \times B^2$. Then, corresponding to each Φ_B^γ with CS ratio γ , we adopt the first M_B^γ columns from PBM as the projection matrix \mathbf{W}_B^γ , i.e., $\mathbf{W}_B^\gamma = \mathbf{W}[:, :M_B^\gamma]$, which is of size $d \times M_B^\gamma$. Obviously, we only need to jointly train the PBM \mathbf{W} once, rather than train B^2 different projection matrices for B^2 times, making our FLP much more flexible. Therefore, as illustrated in Fig. 5(a), the output of our FLP layer, denoted by \mathbf{Z}^0 , can be formulated as:

$$\mathbf{Z}^0 = \mathbf{Q} + \mathbf{P} = \mathbf{W}_B^\gamma \mathbf{Y} + \mathbf{P}, \quad (8)$$

where $\mathbf{Z}^0 \in \mathbb{R}^{d \times L}$. Note that an extra class token exists in the image classification task concatenated with \mathbf{Z}^0 going through the transformer encoder to collect the category information for prediction. The class token is inherited from [37] and has been widely used in recent transformer-based image classification researches [49], [50], [51].

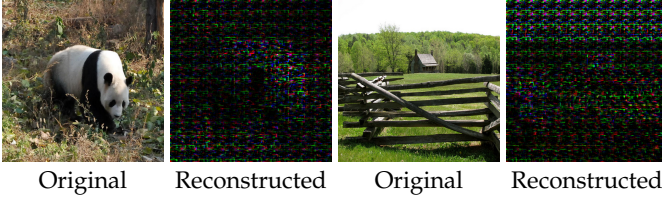


Fig. 8. Visualization of privacy protection. We present the original image and reconstructed result generated by [61] without knowing the sampling matrix.

Transformer Encoder. Taking the embedding sequence \mathbf{Z}^0 as input, the transformer encoder (TE), constructed by a stack of pure transformer layers [36] as shown in Fig. 5(a), is deployed to extract deeper features from the CS measurements. The core part of each transformer layer is a multiheaded self-attention (MSA) block. Each head performs the operation defined in Eq. (3), and their outputs are concatenated together. Multilayer perceptrons (MLP), Layer Norm (LN), and residual connections are applied in the tail of each transformer layer. Thus, the output of each transformer layer has the following formulation:

$$\begin{cases} \tilde{\mathbf{Z}}^l = \text{MSA}(\text{LN}(\mathbf{Z}^l)); \\ \mathbf{Z}^{l+1} = \text{MLP}(\text{LN}(\tilde{\mathbf{Z}}^l)) + \tilde{\mathbf{Z}}^l, \quad l = 0, 1, 2, \dots, K-1, \end{cases} \quad (9)$$

where K is the number of transformer layers (12 by default), and \mathbf{Z}^K denotes the output of TE.

3.4 Task-oriented Head

Our TransCL focuses on two high-level vision tasks: image classification and semantic segmentation. For each task, we adopt a specific task-oriented head (TH) to process \mathbf{Z}^K .

3.4.1 Task-oriented Head for Image Classification

As illustrated in Fig. 5(b), the task-oriented head for image classification (THIC) is a simple combination of linear projection and layer norm. The input of THIC is the learnable class token (*i.e.*, $\mathbf{Z}^K[:, 0]$) with the vector length being 768, and then the classification head performs a prediction on the top of the class token. Note that the class token only exists in the image classification task.

3.4.2 Task-oriented Head for Semantic Segmentation

The task-oriented head for semantic segmentation (THSS) follows the same architecture as the recent transformer-based method [54], which takes the original image as input and is also the upper bound model of our TransCL in this task. Since we obtain measurements in an image block of size 16×16 , the size of \mathbf{Z}^K is $\frac{W}{16} \times \frac{H}{16}$. Through THSS, \mathbf{Z}^K is then gradually upsampled to a segmentation map with the same size as the original image. As illustrated in Fig. 5(c), THSS is essentially a simple progressive upsampling model without any bells and whistles. Specifically, each upsampling block is a triple combination of a 1×1 convolutional layer, a Synchronized BatchNorm, and a ReLU [64] activation function ending with a bilinear upsampling operation. The simplicity of THSS can also better demonstrate the effectiveness of our proposed TransCL.

3.5 Privacy Protection

It is worth emphasizing that our TransCL is superior in privacy protection. On the one hand, the CS measurements have little visual information, which is an inherent property of CS. Although there exist several CS reconstruction methods, *e.g.*, [12], [13], [61], [65], they all need to know the corresponding sampling matrix, especially at low CS ratios. To verify it, we adopt the recent [61] for reconstruction with the CS measurements generated by our trained CSM rather than its own learned sampling matrix. The reconstructed results are presented in Fig. 8, from which one can observe that it is almost inaccessible to original images without the corresponding sampling matrix. On the other hand, the transformer-based backbone (TB) in our TransCL can further strengthen the ability of privacy protection due to the serialized intermediate features, which are more abstract and invisible than CNN counterparts. Thus, we believe that our TransCL can protect data privacy in the process of data transmission and processing.

4 EXPERIMENT

To demonstrate the superiority of our proposed TransCL, we apply it to two representative high-level vision tasks, *i.e.*, image classification and semantic segmentation. The experiment design comes from two factors. On the one hand, studying several linear projection layers under traditional problem settings with tiny images has little significance for promoting CL. The urgent problem faced by CL is how to handle real-world benchmarks and perform inference as flexibly as image-domain methods. On the other hand, though our approach is a new formulation of CL under new problem settings, only comparing our TransCL with image-domain methods on real-world benchmarks is inadequate. We also need to compare our TransCL with existing CL methods (*i.e.*, VCL [66] and MCL [30]), which are difficult to handle large-scale images. Thus, in the experiment, we focus on comparing our TransCL with the recent image-domain methods to present that CL can also be applied to complex and real-world benchmarks (*e.g.*, ImageNet [67], ADE20K [68], PASCAL Context [69], and Cityscapes [70]) without rigid restrictions from data scale and CS ratio. Additionally, we also train and evaluate our TransCL on tiny datasets (*e.g.*, CIFAR10 and CIFAR100 [33]) to directly compare with existing CL methods.

4.1 Model Details and Variants

In image classification, the transformer architecture is the same as the base vision transformer (ViT-B), which contains 12 transformer layers, with the number of heads being 12 in each layer. The dimension of the measurement embedding \mathbf{Q} is set as 768. In semantic segmentation, we utilize the same backbone (ViT-L) as the upper-bound model (SETR). It contains 24 transformer layers, with the number of heads being 16. The dimension of the measurement embedding \mathbf{Q} is set as 1024. Several variants of our proposed TransCL are defined with different names. For instance, “TransCL-16-10” represents the variant with the block size of 16×16 and CS ratio of 10%. In our experiments, we evaluate our TransCL with both fixed CS ratios and arbitrary CS ratios. The fixed CS ratios include 10%, 5%, 2.5%, and 1%. We denote *arb* as

the suffix of the variant that can handle input measurements with arbitrary CS ratios. The suffixes of block size include 16 and 32.

4.2 Image Classification

Experiment Settings. Image classification is the most representative high-level vision task. For this application, we apply our model to the ImageNet 2012 [67], CIFAR-10, and CIFAR-100 [33] datasets:

- **ImageNet 2012** contains 1.28 million training images and 50,000 validation images from 1,000 categories. The image resolution is set as 384×384 . It is a commonly used benchmark in the image domain. However, limited by the computational cost, little CL method can be applied to this dataset at such scale.
- **CIFAR-10** consists of 60,000 32×32 colour images in 10 classes, with 6,000 images per class. There are 50,000 training images and 10,000 test images.
- **CIFAR-100** is just like the CIFAR-10, except it has 100 classes. For each class, there are 500 training images and 100 testing images.

Note that CIFAR-10 and CIFAR-100 are two datasets with tiny images. The transformer architecture has difficulty in processing tiny input. ViT [49] upsampled images from these two datasets and then performed inference. Considering the upsampling will introduce additional information into CS measurements, we interpolate the measurements $\mathbf{Y} (\mathbb{R}^{M_B^\gamma \times L'} \mapsto \mathbb{R}^{M_B^\beta \times L})$ instead of the input images. In this way, no extra information is involved in the measurements. During training, we apply the same training settings as the upper bound model (ViT-B [49]) of our TransCL. Specifically, we use SGD with momentum being 0.9 and the weight-decay being 10^{-4} as the optimizer. The batch size is set as 256, and we train our proposed TransCL on 4 NVIDIA V100 GPUs. Realizing the importance of the pre-trained model in transformer-based methods, we initialize the parameters in TB with the pre-trained model of ViT-B. The CSM, TB, and TH in TransCL are jointly optimized by a cross-entropy loss. Moreover, traditional ViT requires large-scale datasets (*e.g.*, ImageNet-21K) for pre-training. Recently, some strategies were proposed to build data-efficient ViT. For instance, the timm [71] presents a training procedure to improve the top-1 accuracy of ViT-B from 77.91% to 79.35% with ImageNet-1K only. The recent DeiT [50] utilizes a more elaborate optimization process and knowledge distillation strategies to further improve the performance. Inspired by DeiT, in this paper, we also present a data-efficient version (*i.e.*, \aleph), which is trained with knowledge distillation on ImageNet-1K only. The distillation process and teacher network follow the same design as DeiT.

Comparison Results. The evaluation is conducted on the large-scale ImageNet and tiny CIFAR-10/100 datasets. We compare our TransCL with some image-domain methods, *e.g.*, the well-known ResNet [72] and transformer-based methods [49], [50], [53], [73]. We also compare our method with existing CL methods, *i.e.*, VCL [66] and MCL [30], [31]. To fully demonstrate the superiority of our method, we also replace the CNN-based backbone in VCL and MCL with ViT-B model, dubbed VCL-T and MCL-T, respectively. We apply the same training settings to optimize these two models. We report the comparison results of different methods

TABLE 1

Image classification performance on validation dataset of ImageNet. “Top-1 ACC” denotes the top-1 (%) accuracy. Performances of different methods, model parameters, and the number of measurements for each image are reported.

Method	Meas.	Param./Flops	Top-1 ACC
ResNet-18 [72]	3×50176	12M/1.9G	69.83
ResNet-50 [72]	3×50176	25M/4.2G	76.20
ResNet-101 [72]	3×50176	45M/7.8G	77.41
ResNet-152 [72]	3×50176	60M/11.58G	78.33
ViT-B-16 [49]	3×147456	86M/49.3G	83.97
ViT-B-32 [49]	3×147456	88M/12.3G	81.28
PVT-Large [53]	3×50176	62M/9.9G	81.71
DeiT-B \uparrow 384 [50]	3×147456	86M/49.4G	83.12
Twins [73]	3×50176	99M/14.8G	83.70
VCL-T-10	3×14745	589M/50.8	67.59
VCL-T-1	3×1474	136M/49.6	59.89
MCL-T-10	3×14770	87M/49.4	74.07
MCL-T-1	3×1477	86M/49.3	68.92
TransCL-16,32-10	3×14745	86,88M/49.3,12.3G	83.86,81.82
TransCL-16,32-5	3×7372	86,88M/49.3,12.3G	83.05,81.53
TransCL-16,32-2.5	3×3686	86,88M/49.3,12.3G	81.34,80.50
TransCL-16,32-1	3×1474	86,88M/49.3,12.3G	78.86,78.00
TransCL-16-10 \aleph	3×14745	86M/49.3G	83.29
TransCL-16-5 \aleph	3×7372	86M/49.3G	82.46
TransCL-16-2.5 \aleph	3×3686	86M/49.3G	81.24
TransCL-16-1 \aleph	3×1474	86M/49.3G	78.58

TABLE 2

Image classification performance on validation datasets of CIFAR-10 and CIFAR-100 [33]. Top-1 (%) accuracy is presented below.

CS Ratio	Method	Backbone	Meas.	CIFAR -10	CIFAR -100
25%	VCL [66]	ResNet110	768	78.56	53.03
	MCL [30]	ResNet110	760	89.22	67.21
	VCL-T	ViT-B-32	768	93.80	78.65
	MCL-T	ViT-B-32	760	94.51	78.60
	TransCL-16	ViT-B-16	760	94.35	81.45
	TransCL-32	ViT-B-32	760	95.18	82.33
10%	VCL [66]	ResNet110	306	67.65	47.90
	MCL [30]	ResNet110	308	84.74	60.30
	MCLwP [31]	AllCNN [74]	308	85.84	59.83
	VCL-T	ViT-B-32	306	89.22	70.22
	MCL-T	ViT-B-32	308	90.16	67.53
	TransCL-16	ViT-B-16	306	90.66	72.80
TransCL-32	ViT-B-32	306	91.57	72.11	
1.8%	VCL [66]	ResNet110	54	61.96	41.03
	MCL [30]	ResNet110	54	64.14	33.67
	VCL-T	ViT-B-32	54	61.96	41.86
	MCL-T	ViT-B-32	54	62.28	36.43
	TransCL-16	ViT-B-16	54	68.44	42.66
	TransCL-32	ViT-B-32	54	69.60	42.75

on the ImageNet validation set in Tab. 1. One can see that compared with image-domain methods, our proposed TransCL achieves state-of-the-art performance while utilizing significantly fewer measurements. Even if only 1% measurements are available, our TransCL can still achieve 78.86% classification accuracy. Furthermore, our data-efficient version (*i.e.*, \aleph) can achieve comparable performance, trained on the ImageNet-1K only. VCL-T and MCL-T can not perform well on such large-scale benchmarks, and they produce a lot of extra computational complexity. More details can be found in Sec. 5.3. The evaluation on tiny CIFAR-10/100 datasets is mainly used to compare our method with existing CL methods. Note that the measurement results of VCL-T and MCL-T are tensors with the same size (32×32) as the input, which is not suitable as input of ViT. We utilize bilinear upsampling to resize them to 384×384

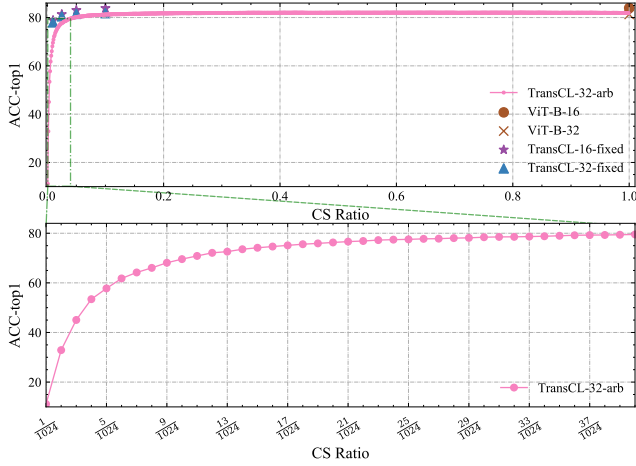


Fig. 9. Image classification performance of a single model (TransCL-32-arb) for handling input with arbitrary CS ratios. The first row presents the performance comparison in the case of input with a fixed CS ratio and arbitrary CS ratios. The second row is a partial enlargement of the region labeled with a green box in the first row, presenting the high robustness of our method in handling extremely low and arbitrary CS ratios.

and then feed them to the ViT backbone. The results are presented in Tab. 2, presenting that our TransCL significantly outperforms recent top-performing CL methods [30], [31]. In addition, as the number of categories increases or the CS ratio decreases, the margin in performance gains of our proposed TransCL becomes greater. The results in Tab. 1 and Tab. 2 demonstrate that our proposed TransCL performs well on high-resolution images with large visual redundancy and tiny images with intensive information.

Performance with arbitrary CS ratios. Handling measurements with arbitrary CS ratios is valuable and practical, but it has not been explored in existing CL tasks. In this part, we study image classification performance in the case of input measurements with arbitrary CS ratios. The classification performance is presented in Fig. 9. We can find that our proposed TransCL can handle 1,024 different CS ratios ($\gamma \in [\frac{1}{1024}, 1]$) with a single model while maintaining stable performance. The enlarged local part in the second row of Fig. 9 shows that the performance of our TransCL rapidly reaches the peak with the increase of CS ratio and then becomes stable. In the extreme case where the CS ratio is $\frac{1}{1024}$ (only about 148 measurements are available for each 384×384 image), our TransCL can still achieve 12% classification accuracy of 1,000 categories. In addition, compared with the variants at fixed CS ratios, the performance loss is minimal, presenting the strong robustness of our TransCL.

4.3 Semantic Segmentation

Experiment Settings. For the application of semantic segmentation, we conduct experiments on the following three widely-used benchmarks:

- **Cityscapes** [70] has 19 annotated object categories in street scenes from 50 different cities. It contains 5,000 annotated images in which 2,975 images for training, 500 images for validation, and 1,525 images for testing. The images are in high resolution with the size being 2048×1024 .

TABLE 3
Quantitative comparison of semantic segmentation task on ADE20K [68] dataset. Performances of different methods and the number of measurements for each image are reported.

Methods (Backbone)	Meas.	Param./Flops	mIoU/Acc
PSP [75] (ResNet-269)	3×223729	73M/246G	44.94/81.69
GFF [76] (ResNet-101)	3×262144	141M/811G	45.33/-
APC [77] (ResNet-101)	3×331776	76M/357G	45.38/-
Twins [73] (SVT-L)	3×262144	133M/297G	48.80/-
SETR [54] (ViT-L-16)	3×262144	309M/316G	50.28/83.46
Ours (TransCL-16-10)	3×26214	309M/316G	50.00/83.51
Ours (TransCL-16-5)	3×13107	309M/316G	49.96/83.44
Ours (TransCL-16-2.5)	3×6553	309M/316G	48.60/83.13
Ours (TransCL-16-1)	3×2621	309M/316G	46.57/82.14

TABLE 4
Quantitative comparison of semantic segmentation task on Cityscapes [70] dataset. Performances of different methods and the number of measurements for each image are reported.

Methods (Backbone)	Meas.	Param./Flops	mIoU
PSP [75] (ResNet-101)	3×508369	73M/554G	78.50
CCNet [78] (ResNet-101)	3×591361	71M/698G	80.20
GFF [76] (ResNet-101)	3×746496	141M/2305G	80.40
SETR [54] (ViT-L-16)	3×589825	309M/818G	82.15
Ours (TransCL-16-10)	3×58982	309M/818G	82.02
Ours (TransCL-16-5)	3×29491	309M/818G	81.73
Ours (TransCL-16-2.5)	3×14745	309M/818G	81.53
Ours (TransCL-16-1)	3×5898	309M/818G	79.29

- **ADE20K** [68] is a challenging benchmark with 150 annotated object categories, which has 20210 training pairs, 2000 validation pairs, and 3352 testing pairs.
- **PASCAL Context** [69] has 60 annotated object categories (59 classes and 1 background). It has 4998 training pairs and 5105 validation pairs.

As mentioned above, SETR [54] is the upper-bound model of our TransCL in image domain in this application. Thus, we apply the same training strategy as SETR. Specifically, at the beginning of training, we utilize the pre-trained parameters of ViT-L-16 [49] in the image classification task to initialize parameters in TB. Then we use the default setting of public codebase mmsegmentation [79] to train our TransCL. Concretely, the input image is randomly resized with the ratio between 0.5 and 2 and randomly cropped with the size being 768, 512, and 480 for Cityscapes, ADE20K, and Pascal Context, respectively. A random horizontal flipping is also applied during training. We train the network on these three benchmarks with the batch size being 8, 16, and 8, respectively. We adopt a polynomial learning rate decay schedule [75] and employ SGD as the optimizer during training. The momentum and weight decay are set to 0.9 and 0, respectively. We set the initial learning rate as 0.001 on ADE20K and Pascal Context and 0.01 on Cityscapes. The CSM, TB, and TH in TransCL are jointly optimized by a pixel-wise cross-entropy loss.

Comparison Results. In this application, we focus on comparing our proposed TransCL with its upper bound model [54] and some state-of-the-art methods [73], [75], [76], [77], [78] in image domain. The quantitative comparison of semantic segmentation on ADE20k [68], Cityscapes [70], and Pascal Context [69] are presented in Tab. 3, Tab. 4, and Tab. 5, respectively. Clearly, our method can achieve comparable performance to SETR [54] and outperform some

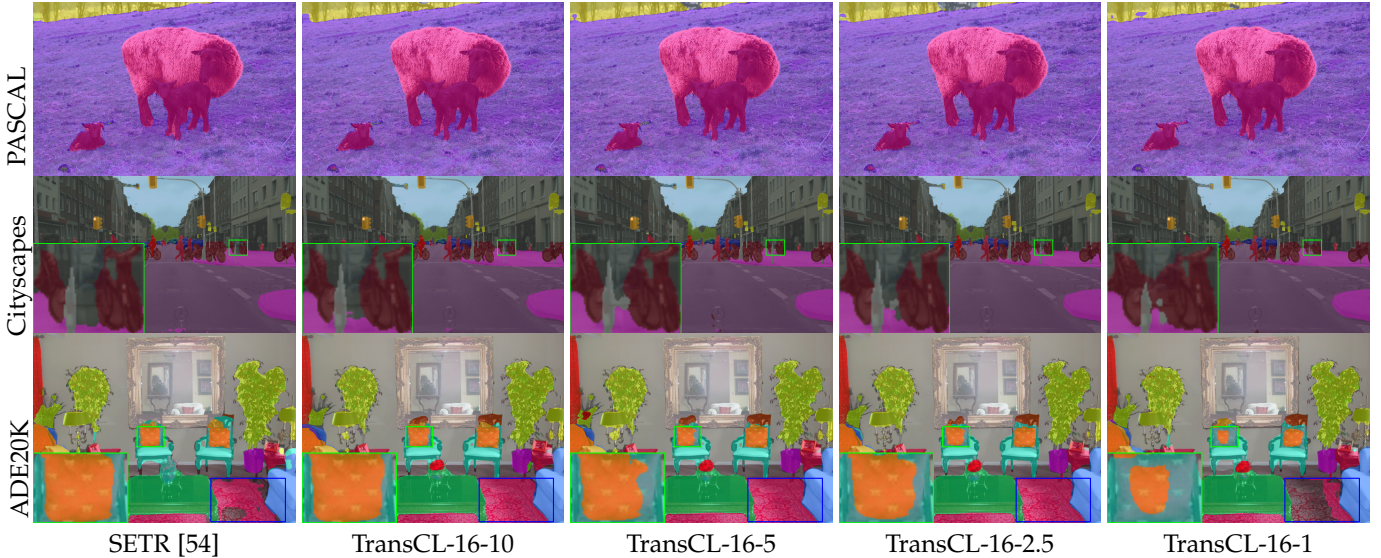


Fig. 10. Visual comparison of semantic segmentation. We visualize the segmentation result of samples from PASCAL Context [69], Cityscapes [70], and ADE20K [68], which are presented in the first row, the second row, and the third row, respectively.

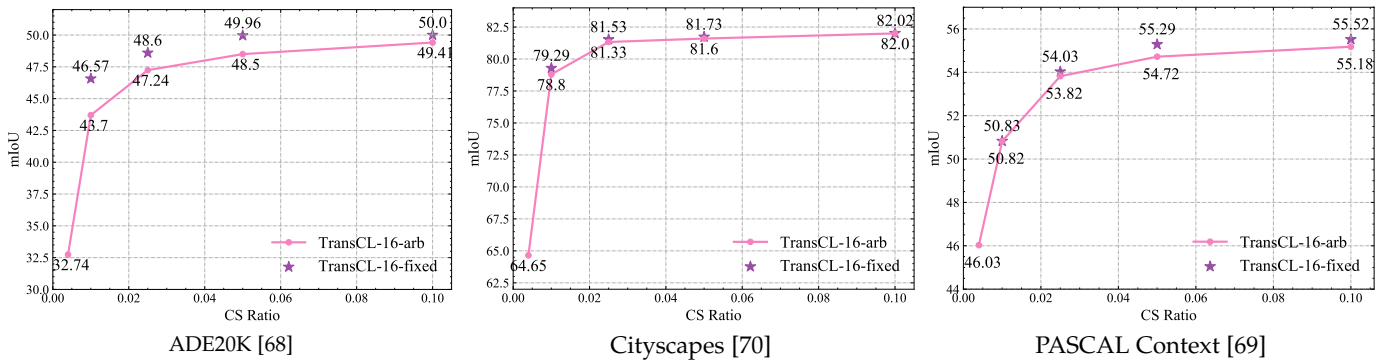


Fig. 11. Semantic segmentation performance of our TransCL with arbitrary CS ratios on three benchmarks.

TABLE 5

Quantitative comparison of semantic segmentation task on Pascal Context [69] dataset. Performances of different methods and the number of measurements for each image are reported.

Methods (Backbone)	Meas.	Param./Flops	mIoU
PSP [75] (ResNet-101)	3 × 223729	73M/246G	47.80
GFF [76] (ResNet-101)	3 × 262144	141M/811G	54.20
APC [77] (ResNet-101)	3 × 262144	76M/282G	54.70
SETR [54] (ViT-L-16)	3 × 230400	309M/281G	55.83
Ours (TransCL-16-10)	3 × 23040	309M/281G	55.52
Ours (TransCL-16-5)	3 × 11520	309M/281G	55.29
Ours (TransCL-16-2.5)	3 × 5760	309M/281G	54.03
Ours (TransCL-16-1)	3 × 2304	309M/281G	51.83

state-of-the-art image-domain methods with significantly fewer measurements. The visualization comparison on three benchmarks is presented in Fig. 10, presenting the attractive semantic segmentation results of our methods. Specifically, in scenarios with few objects (*e.g.*, the first row and second row of Fig. 10), our TransCL can achieve comparable performance to [54] with much fewer measurements. As presented in the third row of Fig. 10, our TransCL maintains superior performance in the challenging ADE20K benchmark, which contains 150 annotated object categories.

Performance with Arbitrary CS Ratios. In semantic segmentation, we also study the performance of our Tran-

sCL in the challenging setting with arbitrary CS ratios. The block size is set as 16×16 . Thus, our TransCL can handle 256 different CS ratios ($\gamma \in [\frac{1}{256}, 1]$) with a single model. We present the segmentation performance in Fig. 11, presenting that the performance rapidly improves with the increase of CS ratio and then becomes stable. There is only a slight performance decrease compared with the model trained with fixed CS ratios. Note that in the challenging ADE20K [68], our proposed method can still maintain stable performance with arbitrary CS ratios. In the extreme case with the CS ratio being $\frac{1}{256}$, our proposed TransCL can still achieve satisfactory results on these three benchmarks. These results fully demonstrate that our proposed TransCL can perform complex high-level vision tasks in the measurement domain with state-of-the-art performance and robustly handle arbitrary CS ratios with a single model.

5 ABLATION STUDY AND DISCUSSIONS

In this section, we focus on studying the effectiveness of different components in our TransCL and presenting some superior properties and interesting findings of our TransCL.

5.1 Comparison with CNN Counterpart

Non-local self-similarity is an effective prior in compensating for the information loss and resisting inference due to

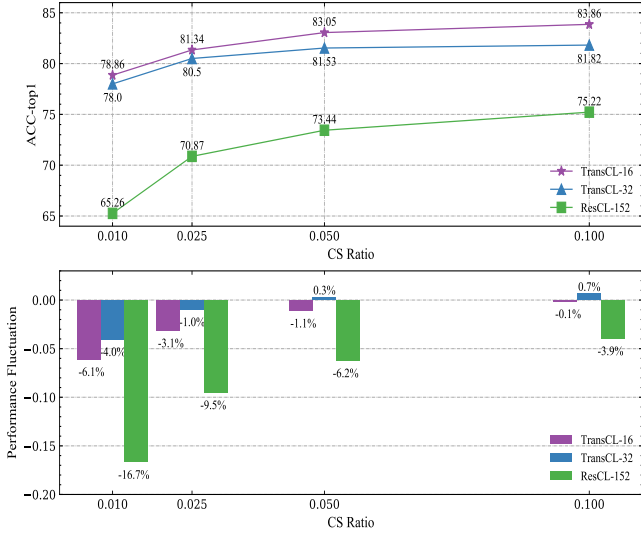


Fig. 12. Image classification performance comparison between our proposed TransCL and its CNN counterpart (ResCL) at different CS ratios and the performance changes compared with their upper bound model. The results reflect the advantages of our proposed TransCL in performance and stability.

its robust capacity in constructing long-range correlations. To demonstrate its effectiveness in CL tasks, we compare our TransCL with its CNN counterpart. Specifically, we replace the transformer-based backbone (TB) in TransCL with the very deep ResNet-152 [72] (represented as ResCL). We evaluate the performance of our TransCL and ResCL under various conditions in the image classification task. Note that the serialized input is intractable to the CNN architecture. Thus, we combine the input sequence into a square tensor in which each vectorized measurement is located in the position of the original image block.

5.1.1 Performance and Stability

The comparison is conducted on ImageNet 2012 [67] dataset with the CS ratios being 1%, 2.5%, 5%, and 10%. We report the top-1 (%) classification accuracy of our TransCL and ResCL at different CS ratios and present the performance changes (%) compared with their upper bound models (ViT-B [49] and ResNet-152) in the first row and second row of Fig. 12, respectively. Clearly, our TransCL enjoys advantages in both performance and stability. Specifically, our proposed TransCL performs better than ResCL in all evaluation points, and the margin becomes larger as the decrease of CS ratio. The stability of our TransCL is reflected in two aspects, *i.e.*, the performance decays more slowly and is closer to the upper bound model.

5.1.2 Resisting Noise Perturbation

In the process of CS, there usually exists noise perturbation from the natural environment and hardware. [25] exploited the performance bound of CL under the noise perturbation. In this part, we study the capacity of our TransCL and ResCL to resist the noise perturbation. Following [25], we add random Gaussian noise $\mathbf{n} \sim \mathcal{N}(\mu, \sigma^2)$ to original images. The CS process is correspondingly expressed as:

$$\mathbf{y}_i = \Phi_B^\gamma \mathbf{x}_i + \Phi_B^\gamma \mathbf{n}. \quad (10)$$

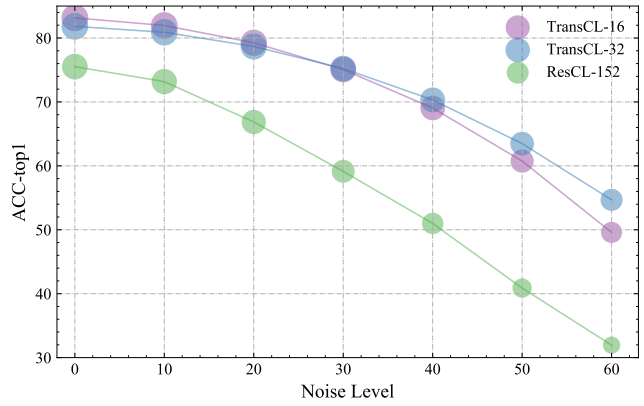


Fig. 13. The comparison of ability to resist noise perturbation of our TransCL and its CNN counterpart (ResCL). We present the top-1 (%) accuracy on ImageNet validation set with the Gaussian noise level $\sigma \in \{0, 10, 20, \dots, 60\}$.

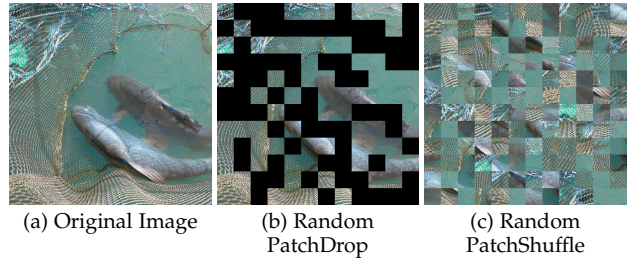


Fig. 14. Visualization of disturbing patterns, including random PatchDrop and random PatchShuffle.

In the experiment, we utilize the zero-mean Gaussian noise and set the CS ratio as 10%. Note that all methods are trained with clean images, and we only add the noisy signal in the evaluation. We evaluate the performance under noise perturbation with different noise levels on the ImageNet validation set and present the comparison result in Fig. 13. Obviously, our proposed TransCL performs better than ResCL, demonstrating the effectiveness of the transformer-based backbone. We can also find that TransCL-32 performs better than TransCL-16, which can be interpreted by the fact that the TransCL-32 has a larger receptive field of matching patches leading to more robust long-range correlations to resist noisy signals.

TABLE 6
Quantitative comparison of two-stage method and our single-stage TransCL on image classification task. We present the top-1 (%) accuracy on ImageNet validation set in this table.

Type	Method	CS ratio			
		10%	5%	2.5%	1%
Two-stage	OPINE-Net ⁺ [61]	80.65	77.00	70.89	55.57
	ViT-B-32 [49]	80.65	77.00	70.89	55.57
Single-stage	TransCL-32 (Ours)	81.82	81.53	80.50	78.00

5.1.3 Resisting Random PatchDrop and PatchShuffle

To further demonstrate the superiority of our TransCL in resisting information loss and external interference, we deploy two types of interference, *i.e.*, Random PatchDrop and Random PatchShuffle, which are only added during testing. As shown in Fig. 14(b), for Random PatchDrop, we randomly

TABLE 7

Comparison of complexity of various strategies to infer a 384×384 image and the top-1 (%) accuracy on ImageNet [67] validation set. The additional complexity produced in measurement reconstruction stage is highlighted in red.

Methods	ResCL-152	ResCL-101	ResCL-50	DensCL-201	DensCL-121	Two Stages	TransCL-16	TransCL-32
Speed (ms/image)	16.9	11.9	7.5	11.9	8.4	7.4+25.2	30.15	7.4
Peak Memory (GB)	2.2	1.9	1.5	2.3	1.7	max(1.5, 6.8)	3.2	1.5
Param. (M)	60	45	25	20	8	88+0.6	86	88
Flops (G)	30.1	23.0	12.1	12.8	8.4	12.3+112	49.3	12.3
Accuracy (%)	75.22	71.77	70.19	72.05	69.23	80.65	83.36	81.82

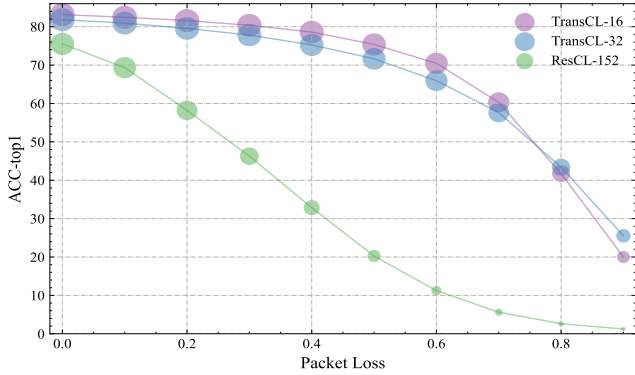


Fig. 15. The comparison of resisting random PatchDrop of our TransCL and its CNN counterpart (ResCL) on ImageNet validation set with various packet losses.

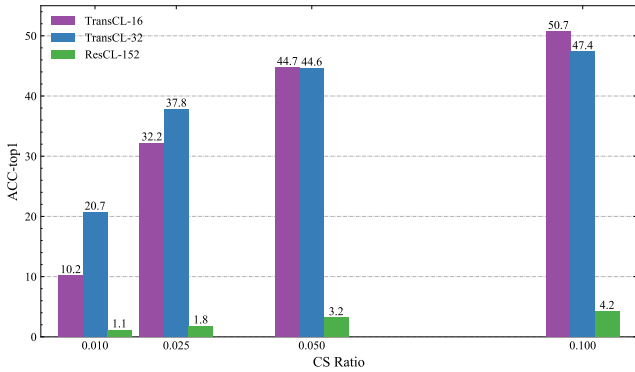


Fig. 16. Top-1 (%) accuracy over ImageNet validation set with shuffled image patches. We compare our TransCL with its CNN counterpart (ResCL).

mask some square regions of the block-based compressed sensing (BCS) process with a certain proportion to simulate the packet loss during data transmission. The evaluation results are presented in Fig. 15, presenting that our proposed TransCL performs better than the ResCL with a large margin. This benefits from the fact that transformer can fully utilize the non-local property in sequence, rather than operating within a local region. For Random PatchShuffle, we eliminate the structural information within images by defining a shuffling operation on input image patches. One sample of this operation is presented in Fig. 14(c), whose spatial structure is badly damaged. This setting can simulate data transmission in the wrong sequence. The evaluation results are presented in Fig. 16, from which one can observe that the resistance ability of our TransCL to this interferential factor is obviously better than ResCL.

5.2 Comparison with Two-stage Method

As illustrated in Fig. 2, a straightforward method to solve high-level vision tasks with CS measurements is reconstructing first and then inferring. However, this strategy potentially discloses private information and has computational redundancy, *i.e.*, in many applications, we are not interested in obtaining a precise reconstruction of the scene under view, but rather are only interested in the results of inference tasks. In this part, we provide experimental results to demonstrate that the reconstruction step is almost unnecessary, and our proposed TransCL can achieve better performance with a single stage. In terms of the implementation of the two-stage method, we apply the top-performing method [61] as the reconstruction module. Then we use ViT-B-32 [49] to perform image classification based on the reconstruction output. We set the CS ratio as 10%, 5%, 2.5%, and 1%. The comparison result on ImageNet validation set is presented in Tab. 6. One can see that the two-stage method has satisfied performance with high CS ratios, but the performance declines sharply with the decrease of CS ratio. It indicates that there exists serious coupling problem between the reconstruction model and inference model, *i.e.*, the inference model trained with natural images can not adapt the input from CS restoration results. Therefore, for a satisfactory result, we need jointly optimize a specific restoration model and an inference model at each CS ratio, which is not feasible in practical applications. By contrast, our proposed TransCL can achieve attractive and stable performance without coupling problem while also having the advantage of privacy protection.

TABLE 8

Quantitative comparison of our compressive learning method with traditional data compression approaches on image classification task. We present the top-1 (%) accuracy on ImageNet validation set.

Sampling ratio	10%	5%	2.5%	1%
SVD+ViT-B-32 [49] (w/o re-training)	68.69	42.02	12.08	2.7
Bicubic+ViT-B-32 [49] (w/o re-training)	74.00	68.24	60.12	42.51
Bicubic+ViT-B-32 [49]	81.00	80.03	78.48	73.91
TransCL-32	81.82	81.53	80.50	78.00

5.3 Complexity Analysis

As illustrated in Fig. 2, since no signal reconstruction is required, CL is an efficient way to perform high-level vision tasks in the measurement domain and should runs faster than two-stage methods (reconstruct and then infer). Additionally, the transformer-based backbone is efficient in data

processing, which has been studied in ViT [49] (please refer to Fig.11 in [49]). Thus, in this part, we focus on analyzing the model complexity of CL and two-stage strategy, and we compare our proposed TransCL with some CNN counterparts, *i.e.*, ResCL and DensCL. Note that the implementation of two-stage method is the same as Tab. 6. In the experiment, we set the image size and CS ratio as 384×384 and 10%, respectively. The evaluation results of inference speed, peak memory, parameters, and Flops are presented in Tab. 7, which are all evaluated on an NVIDIA TESLA T4 GPU. We also present the top-1 accuracy of each strategy on ImageNet validation set in this table. We can find that compared with some commonly used CNN-based backbones, our TransCL has advantages in terms of inference speed and Flops, and the efficiency is more obvious when compared with the two-stage strategy. Specifically, the time complexity and Flops of our TransCL-32 are significantly lower than the ResNet-152 and ResNet-101 and achieve comparable inference speed with the tiny ResNet-50. This property mainly benefits from the efficiency of dot products on GPU. In the two-stage strategy, the restoration model produces $3.4 \times$ time complexity, $4.3 \times$ peak memory, and $9.1 \times$ flops even with much fewer parameters. This is because the reconstruction process is a pixel-to-pixel projection without changing spatial size. Thus, given a 384×384 input, the reconstruction model demands a high computational burden. Due to the four times length of the input sequence, TransCL-16 has higher model complexity than TransCL-32. The performance gains are also obvious compared with other strategies.

We present the model complexity of different CL methods to measure a 384×384 image with the CS ratio being 1% in Tab. 9. We can find that VCL and MCL produce a lot of extra computational complexity in handling large-scale images. Such additional model complexity is unnecessary and makes them difficult to deal with real-world benchmarks.

TABLE 9

Complexity comparison of various CL methods to sample a 384×384 color image, with the CS ratio being 1%.

	VCL [66]	MCL [30]	TransCL (Ours)
Parameters	2.0×10^9	1.1×10^5	2.7×10^3
Flops	1.3×10^9	4.6×10^7	2.6×10^6

5.4 Comparison with Traditional Data Compression Methods

In this part, we want to show that learning in the measurement domain better preserves image information than the conventional data compression approaches. We compare our TransCL with the spatial downsampling and SVD [80] methods. Specifically, for spatial downsampling, we utilize the bicubic algorithm to downsample the input image with the same ratio as the compressed sensing operation in our TransCL. Then, we utilize bilinear interpolation to resize the downsampled image to the original scale. To make a fair comparison, we also re-train a specific ViT-B model on ImageNet 2012 dataset for each downsampling factor, and the training strategy is the same as that we use to train our TransCL. For SVD compression, we decompose the input image by the SVD algorithm and then retain a specific amount of data according to the sampling ratio. Concretely,

TABLE 10

Comparison of the float-point sampling matrix and the binary sampling matrix. The result presents that our TransCL has the hardware-friendly property. The image classification task is conducted on TransCL-32, and the semantic segmentation task is conducted on TransCL-16.

	CS Ratio	1%	2.5%	5%	10%
Classification (Top-1 accuracy)	Float-point	78.00	80.50	81.53	81.82
	Binary	76.12	78.90	80.11	80.91
	Δ	-1.88	-1.6	-1.42	-0.09
Segmentation (mIoU)	Float-point	50.83	54.03	55.29	55.52
	Binary	49.80	53.76	54.87	55.47
	Δ	-1.03	-0.27	-0.42	-0.05

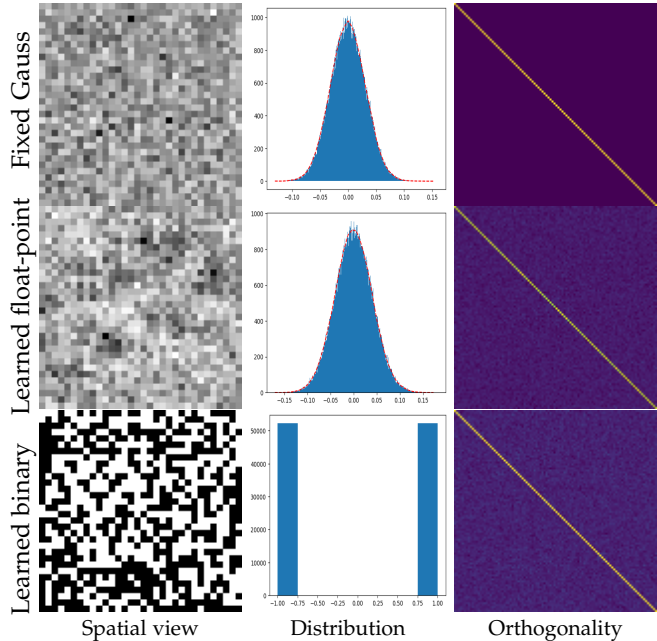


Fig. 17. Visualization of distribution and orthogonality of fixed Gaussian matrix (the first row), learned float-point matrix (the second row), and learned binary matrix (the third row).

given an input image $\mathbf{I} \in \mathbb{R}^{w \times h}$, the SVD algorithm decomposes \mathbf{I} as $\mathbf{I} = \mathbf{u}\mathbf{s}\mathbf{v}$, where $\mathbf{u} \in \mathbb{R}^{w \times w}$ and $\mathbf{v} \in \mathbb{R}^{h \times h}$ are two orthogonal matrixes. $\mathbf{s} \in \mathbb{R}^{w \times h}$ is a diagonal matrix. For data compression, we can retain k columns in \mathbf{u} and k rows in \mathbf{v} according to the singular value in \mathbf{s} . The rebuilding result is defined as $\mathbf{I} = \mathbf{u}_{w \times k} \mathbf{s}_{k \times k} \mathbf{v}_{k \times h}$. The compression ratio is computed as $r = \frac{w \times k + h \times k + k}{w \times h}$. Because the SVD algorithm runs slowly on large-scale data, we only provide the performance of SVD without re-training.

The comparison results are presented in Tab. 8. We can find that the special downsampling and SVD methods are not as efficient as compressive learning. Even though the joint optimization improves the performance of spatial downsampling, our method is still significantly better than the downsampling operation, and the superiority becomes more obvious with the decrease of sampling ratio. Furthermore, the spatial downsampling does not have the property of privacy protection.

5.5 Sampling Matrix

5.5.1 Performance of Binary Sampling Matrix

In this part, we make a performance comparison between learned float-point sampling and learned binary sampling

matrix. The implementation is illustrated in Sec. 3.2 and the experiments are conducted on image classification and semantic segmentation tasks with ImageNet 2012 [67] and Pascal Context [69] datasets, respectively. As shown in Tab. 10, our proposed TransCL can achieve attractive performance with the binary sampling matrix, and there is only a slight performance reduction compared with using the float-point sampling matrix.

5.5.2 Interesting Findings

There are also some interesting findings of the sampling matrix. We take the CS ratio of 0.1 as an example. We reshape one row in a fixed random Gaussian matrix, our learned float-point matrix, and our learned binary matrix into $B \times B$ and visualize their spatial property in the first column of Fig. 17. Moreover, we visualize the distribution and orthogonality $\Phi_B^\gamma (\Phi_B^\gamma)^\top$ of the sampling matrix in the second column and the third column of Fig. 17, respectively. One can see that the learned float-point sampling matrix obeys the Gaussian distribution, which is similar to the commonly used fixed random Gaussian matrix in many previous works [12], [81], [82]. The learned binary matrix has an even distribution at the points of -1 and 1 . Fig. 17 also presents that both float-point and binary sampling matrix is approximately orthogonal, *i.e.*, $\Phi_B^\gamma (\Phi_B^\gamma)^\top \approx \lambda \mathbf{I}$, where $\mathbf{I} \in \mathbb{R}^{M_B^\gamma \times M_B^\gamma}$ is the identity matrix. This property is also consistent with the commonly used fixed random Gaussian matrix. Note that these properties are all learned without specific constraints. These similar characters naturally lead to the following inference: the learned sampling matrix retains the same properties as the fixed random Gaussian matrix, such as RIP [83].

5.6 Discussion: Feature Representation in Measurement Domain and Image Domain

We generally assume that a large margin between measurement domain and image domain exists, and the performance of existing CL methods is not comparable to the image-domain methods. In this paper, we propose a novel CL method to bridge this gap. To further demonstrate our motivation, we visualize the feature representations from the measurement domain and the image domain, respectively. Concretely, we randomly select 50 categories from 1000 categories of the ImageNet validation set, each contains 50 samples. Then we feed these sets of images to pre-trained TransCL-32-10 and ViT-B-32 [49], and we collect the features extracted by these two models. Since the class information is stored in the class token, we utilize T-SNE [84] to reduce the dimensionality of the class token feature of each sample to 2 dimensions for illustration purposes. The results from our TransCL and ViT-B are shown in Fig. 18. We can find that the feature representations generated by our TransCL and ViT-B have good category discrimination, which demonstrates the superiority of our TransCL of better preserving image information from a few measurements. Fig. 18 also presents a high similarity of the feature representations from the measurement domain and image domain. Thus, these two domains are interrelated, and we can bridge the gap through specific designs.

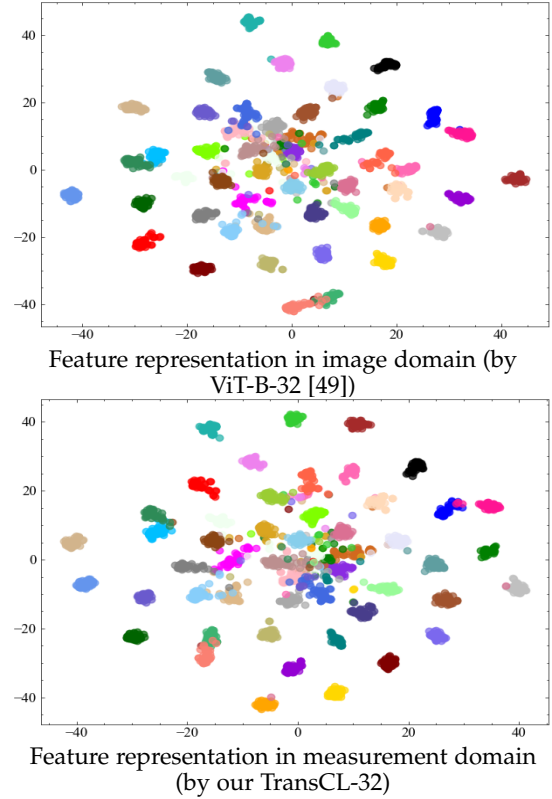


Fig. 18. Visualization of feature representation in measurement domain and image domain. Each figure shows the feature representation after dimension reduction using the T-SNE method [84].

6 CONCLUSION

In this paper, we delve into the high-level visual applications of compressed sensing (CS) beyond the signal reconstruction, presenting that CS reconstruction is almost unnecessary in high-level vision tasks. Technically, we offer a completely new sequence-to-sequence perspective to compressive learning (CL) by applying the block-based compressed sensing (BCS) strategy, and we propose a novel transformer-based CL framework, dubbed TransCL. The proposed TransCL extends the concept of CL to more complex high-level vision tasks and larger datasets with real-world scale, which offers a fresh and successful instance and bridges the gap between inference tasks in the image domain and those in the measurement domain. Furthermore, we study several useful properties of our TransCL in terms of handling arbitrary CS ratios with a single model (Fig. 9 and Fig. 11), good generalization to binary sampling (Tab. 10), robustness under different degradation factors (Sec. 5.1), privacy protection (Fig. 8) and effective data compression (Tab. 8). Extensive experiments and theoretical analysis demonstrate that our proposed TransCL has these superior properties and can achieve state-of-the-art performance in image classification and semantic segmentation tasks, even at extremely low CS ratios. Our future work will focus on designing more efficient sequence-to-sequence CL methods and establishing real-world systems integrated with the hardware.

REFERENCES

[1] E. J. Candès, J. Romberg, and T. Tao, “Robust uncertainty principles: Exact signal reconstruction from highly incomplete fre-

- quency information," *IEEE Transactions on Information Theory*, vol. 52, pp. 489–509, 2006.
- [2] D. L. Donoho, "Compressed sensing," *IEEE Transactions on Information Theory*, vol. 52, pp. 1289–1306, 2006.
- [3] M. F. Duarte, M. A. Davenport, D. Takhar, J. N. Laska, T. Sun, K. F. Kelly, and R. G. Baraniuk, "Single-pixel imaging via compressive sampling," *IEEE Signal Processing Magazine*, vol. 25, pp. 83–91, 2008.
- [4] F. Rousset, N. Ducros, A. Farina, G. Valentini, C. D'Andrea, and F. Peyrin, "Adaptive basis scan by wavelet prediction for single-pixel imaging," *IEEE Transactions on Computational Imaging*, vol. 3, pp. 36–46, 2016.
- [5] M. Lustig, D. Donoho, and J. M. Pauly, "Sparse mri: The application of compressed sensing for rapid mr imaging," *Magnetic Resonance in Medicine: An Official Journal of the International Society for Magnetic Resonance in Medicine*, vol. 58, pp. 1182–1195, 2007.
- [6] Z. Zhang, T.-P. Jung, S. Makeig, and B. D. Rao, "Compressed sensing for energy-efficient wireless telemonitoring of noninvasive fetal eeg via block sparse bayesian learning," *IEEE Transactions on Biomedical Engineering*, vol. 60, pp. 300–309, 2012.
- [7] S. K. Sharma, E. Lagunas, S. Chatzinotas, and B. Ottersten, "Application of compressive sensing in cognitive radio communications: A survey," *IEEE Communications Surveys Tutorials*, vol. 18, pp. 1838–1860, 2016.
- [8] Z. Wang, H. Zhang, Z. Cheng, B. Chen, and X. Yuan, "Metasci: Scalable and adaptive reconstruction for video compressive sensing," in *Proceedings of the IEEE Conference on Computer Vision and Pattern Recognition (CVPR)*, 2021, pp. 2083–2092.
- [9] Z. Wu, J. Zhang, and C. Mou, "Dense Deep Unfolding Network with 3D-CNN Prior for Snapshot Compressive Imaging," in *Proceedings of International Conference on Computer Vision (ICCV)*, 2021, pp. 4892–4901.
- [10] M. Gupta, A. Agrawal, A. Veeraraghavan, and S. G. Narasimhan, "Flexible voxels for motion-aware videography," in *Proceedings of the European Conference on Computer Vision (ECCV)*, 2010, pp. 100–114.
- [11] D. Reddy, A. Veeraraghavan, and R. Chellappa, "P2c2: Programmable pixel compressive camera for high speed imaging," in *Proceedings of the IEEE Conference on Computer Vision and Pattern Recognition (CVPR)*, 2011, pp. 329–336.
- [12] W. Dong, G. Shi, X. Li, Y. Ma, and F. Huang, "Compressive sensing via nonlocal low-rank regularization," *IEEE Transactions on Image Processing*, vol. 23, pp. 3618–3632, 2014.
- [13] M. Iliadis, L. Spinoulas, and A. K. Katsaggelos, "Deep fully-connected networks for video compressive sensing," *Digital Signal Processing*, vol. 72, pp. 9–18, 2018.
- [14] K. Kulkarni, S. Lohit, P. Turaga, R. Kerviche, and A. Ashok, "Reconnet: Non-iterative reconstruction of images from compressively sensed measurements," in *Proceedings of the IEEE Conference on Computer Vision and Pattern Recognition (CVPR)*, 2016, pp. 449–458.
- [15] S. Mun and J. E. Fowler, "Block compressed sensing of images using directional transforms," in *Proceedings of the IEEE International Conference on Image Processing (ICIP)*, 2009, pp. 3021–3024.
- [16] C. Zhao, S. Ma, and W. Gao, "Image compressive-sensing recovery using structured laplacian sparsity in dct domain and multi-hypothesis prediction," in *Proceedings of IEEE International Conference on Multimedia and Expo (ICME)*, 2014, pp. 1–6.
- [17] C. Zhao, S. Ma, J. Zhang, R. Xiong, and W. Gao, "Video compressive sensing reconstruction via reweighted residual sparsity," *IEEE Transactions on Circuits and Systems for Video Technology*, vol. 27, pp. 1182–1195, 2016.
- [18] D. You, J. Zhang, J. Xie, B. Chen, and S. Ma, "COAST: COntrollable Arbitrary-Sampling NeTwork for Compressive Sensing," *IEEE Transactions on Image Processing*, vol. 30, pp. 6066–6080, 2021.
- [19] J. Song, B. Chen, and J. Zhang, "Memory-Augmented Deep Unfolding Network for Compressive Sensing," in *Proceedings of ACM International Conference on Multimedia (ACM MM)*, 2021.
- [20] P. Mohassel and Y. Zhang, "Secureml: A system for scalable privacy-preserving machine learning," in *Proceedings of the IEEE Symposium on Security and Privacy (SP)*, 2017, pp. 19–38.
- [21] R. Gilad-Bachrach, N. Dowlin, K. Laine, K. Lauter, M. Naehrig, and J. Wernsing, "Cryptonets: Applying neural networks to encrypted data with high throughput and accuracy," in *International Conference on Machine Learning (ICML)*, 2016, pp. 201–210.
- [22] R. Calderbank, S. Jafarpour, and R. Schapire, "Compressed learning: Universal sparse dimensionality reduction and learning in the measurement domain," *Preprint*, 2009. [Online]. Available: <http://citeseerx.ist.psu.edu/viewdoc/download?doi=10.1.1.481.8129&rep=rep1&type=pdf>
- [23] M. A. Davenport, M. F. Duarte, M. B. Wakin, J. N. Laska, D. Takhar, K. F. Kelly, and R. G. Baraniuk, "The smashed filter for compressive classification and target recognition," in *Proceedings of SPIE Computational Imaging*, 2007, pp. 142–153.
- [24] T. Wimalajeewa, H. Chen, and P. K. Varshney, "Performance limits of compressive sensing-based signal classification," *IEEE Transactions on Signal Processing*, vol. 60, pp. 2758–2770, 2012.
- [25] Y. Cui, W. Xu, Y. Wang, J. Lin, and L. Lu, "Performance bounds of compressive classification under perturbation," *Signal Processing*, vol. 180, p. 107855, 2021.
- [26] H. Reberedo, F. Renna, R. Calderbank, and M. R. Rodrigues, "Projections designs for compressive classification," in *Proceedings of the IEEE Global Conference on Signal and Information Processing*, 2013, pp. 1029–1032.
- [27] J. Haupt, R. Castro, R. Nowak, G. Fudge, and A. Yeh, "Compressive sampling for signal classification," in *Proceedings of the Fortieth Asilomar Conference on Signals, Systems and Computers*, 2006, pp. 1430–1434.
- [28] E. Zisselman, A. Adler, and M. Elad, "Compressed learning for image classification: A deep neural network approach," in *Processing, Analyzing and Learning of Images, Shapes, and Forms: Part 1*, ser. Handbook of Numerical Analysis, 2018, pp. 3–17.
- [29] S. Lohit, K. Kulkarni, P. Turaga, J. Wang, and A. C. Sankaranarayanan, "Reconstruction-free inference on compressive measurements," in *Proceedings of the IEEE Conference on Computer Vision and Pattern Recognition Workshops (CVPRW)*, 2015, pp. 16–24.
- [30] D. T. Tran, M. Yamaç, A. Degerli, M. Gabbouj, and A. Iosifidis, "Multilinear compressive learning," *IEEE Transactions on Neural Networks and Learning Systems*, vol. 32, pp. 1512–1524, 2021.
- [31] D. T. Tran, M. Gabbouj, and A. Iosifidis, "Multilinear compressive learning with prior knowledge," *arXiv preprint arXiv:2002.07203*, 2020.
- [32] Y. LeCun, L. Bottou, Y. Bengio, and P. Haffner, "Gradient-based learning applied to document recognition," *Proceedings of the IEEE*, vol. 86, pp. 2278–2324, 1998.
- [33] A. Krizhevsky, G. Hinton *et al.*, "Learning multiple layers of features from tiny images," 2009. [Online]. Available: <http://citeseerx.ist.psu.edu/viewdoc/download?doi=10.1.1.222.9220&rep=rep1&type=pdf>
- [34] A. Buades, B. Coll, and J.-M. Morel, "A non-local algorithm for image denoising," in *Proceedings of the IEEE Conference on Computer Vision and Pattern Recognition (CVPR)*, 2005, pp. 60–65.
- [35] K. Dabov, A. Foi, V. Katkovnik, and K. Egiazarian, "Image denoising by sparse 3-D transform-domain collaborative filtering," *IEEE Transactions on Image Processing*, vol. 16, pp. 2080–2095, 2007.
- [36] A. Vaswani, N. Shazeer, N. Parmar, J. Uszkoreit, L. Jones, A. N. Gomez, L. Kaiser, and I. Polosukhin, "Attention is all you need," in *Proceedings of the Advances in Neural Information Processing Systems (NeurIPS)*, 2017.
- [37] J. Devlin, M.-W. Chang, K. Lee, and K. Toutanova, "Bert: Pre-training of deep bidirectional transformers for language understanding," in *Proceedings of the 2019 Conference of the North American Chapter of the Association for Computational Linguistics: Human Language Technologies*, 2019, pp. 4171–4186.
- [38] A. Radford, K. Narasimhan, T. Salimans, and I. Sutskever, "Improving language understanding by generative pre-training," 2018. [Online]. Available: <https://www.cs.ubc.ca/amuham01/LING530/papers/radford2018improving.pdf>
- [39] Z. Li, Z. Zhang, H. Zhao, R. Wang, K. Chen, M. Utiyama, and E. Sumita, "Text compression-aided transformer encoding," *IEEE Transactions on Pattern Analysis and Machine Intelligence*, vol. 44, pp. 3840–3857, 2021.
- [40] L. Gan, "Block compressed sensing of natural images," in *Proceedings of the International Conference on Digital Signal Processing*, 2007, pp. 403–406.
- [41] X. Gao, J. Zhang, W. Che, X. Fan, and D. Zhao, "Block-based compressive sensing coding of natural images by local structural measurement matrix," in *Proceedings of the IEEE 2015 Data Compression Conference (DCC)*, 2015, pp. 133–142.
- [42] K. Kulkarni and P. Turaga, "Reconstruction-free action inference from compressive imagers," *IEEE Transactions on Pattern Analysis and Machine Intelligence (TPAMI)*, vol. 38, pp. 772–784, 2015.
- [43] S. Lohit, K. Kulkarni, and P. Turaga, "Direct inference on compressive measurements using convolutional neural networks," in *Proceedings of the IEEE International Conference on Image Processing (ICIP)*, 2016, pp. 1913–1917.

- [44] A. Adler, M. Elad, and M. Zibulevsky, "Compressed learning: A deep neural network approach," *arXiv preprint arXiv:1610.09615*, 2016.
- [45] Y. Oike and A. El Gamal, "Cmos image sensor with per-column $\sigma \delta$ adc and programmable compressed sensing," *IEEE Journal of Solid-State Circuits*, vol. 48, pp. 318–328, 2012.
- [46] P. S. Gupta and G. S. Choi, "Programmable compressed sensing using simple deterministic sensing matrices," in *Proceedings of the Optoelectronic Imaging and Multimedia Technology V*, 2018, pp. 74–85.
- [47] D. T. Tran, M. Gabbouj, and A. Iosifidis, "Performance indicator in multilinear compressive learning," in *2020 IEEE Symposium Series on Computational Intelligence (SSCI)*, 2020, pp. 1822–1828.
- [48] X. Wang, R. Girshick, A. Gupta, and K. He, "Non-local neural networks," in *Proceedings of the IEEE Conference on Computer Vision and Pattern Recognition (CVPR)*, 2018, pp. 7794–7803.
- [49] A. Dosovitskiy, L. Beyer, A. Kolesnikov, D. Weissenborn, X. Zhai, T. Unterthiner, M. Dehghani, M. Minderer, G. Heigold, S. Gelly et al., "An image is worth 16x16 words: Transformers for image recognition at scale," in *Proceedings of the International Conference on Learning Representations (ICLR)*, 2020.
- [50] H. Touvron, M. Cord, M. Douze, F. Massa, A. Sablayrolles, and H. Jégou, "Training data-efficient image transformers & distillation through attention," in *Proceedings of the International Conference on Machine Learning (ICML)*, 2021, pp. 10 347–10 357.
- [51] K. Han, A. Xiao, E. Wu, J. Guo, C. Xu, and Y. Wang, "Transformer in transformer," in *Proceedings of the Advances in Neural Information Processing Systems (NeurIPS)*, 2021, pp. 15 908–15 919.
- [52] N. Carion, F. Massa, G. Synnaeve, N. Usunier, A. Kirillov, and S. Zagoruyko, "End-to-end object detection with transformers," in *Proceedings of the European Conference on Computer Vision (ECCV)*, 2020, pp. 213–229.
- [53] W. Wang, E. Xie, X. Li, D.-P. Fan, K. Song, D. Liang, T. Lu, P. Luo, and L. Shao, "Pyramid vision transformer: A versatile backbone for dense prediction without convolutions," in *Proceedings of the IEEE International Conference on Computer Vision (ICCV)*, 2021, pp. 568–578.
- [54] S. Zheng, J. Lu, H. Zhao, X. Zhu, Z. Luo, Y. Wang, Y. Fu, J. Feng, T. Xiang, P. H. Torr, and L. Zhang, "Rethinking semantic segmentation from a sequence-to-sequence perspective with transformers," in *Proceedings of the IEEE Conference on Computer Vision and Pattern Recognition (CVPR)*, 2021, pp. 6881–6890.
- [55] S. Yang, Z. Quan, M. Nie, and W. Yang, "Transpose: Keypoint localization via transformer," in *Proceedings of the IEEE International Conference on Computer Vision (ICCV)*, 2021, pp. 11 802–11 812.
- [56] C. Mou, J. Zhang, X. Fan, H. Liu, and R. Wang, "Cola-net: Collaborative attention network for image restoration," *IEEE Transactions on Multimedia*, 2021.
- [57] F. Yang, H. Yang, J. Fu, H. Lu, and B. Guo, "Learning texture transformer network for image super-resolution," in *Proceedings of the IEEE Conference on Computer Vision and Pattern Recognition (CVPR)*, 2020, pp. 5791–5800.
- [58] H. Chen, Y. Wang, T. Guo, C. Xu, Y. Deng, Z. Liu, S. Ma, C. Xu, C. Xu, and W. Gao, "Pre-trained image processing transformer," in *Proceedings of the IEEE Conference on Computer Vision and Pattern Recognition (CVPR)*, 2021, pp. 12 299–12 310.
- [59] S. Mun, *Block compressed sensing of images and video*. Mississippi State University, 2012.
- [60] I. Noor and E. L. Jacobs, "Adaptive compressive sensing algorithm for video acquisition using a single-pixel camera," *Journal of Electronic Imaging*, vol. 22, p. 021013, 2013.
- [61] J. Zhang, C. Zhao, and W. Gao, "Optimization-inspired compact deep compressive sensing," *IEEE Journal of Selected Topics in Signal Processing (JSTSP)*, vol. 14, pp. 765–774, 2020.
- [62] I. Hubara, M. Courbariaux, D. Soudry, R. El-Yaniv, and Y. Bengio, "Binarized neural networks," in *Proceedings of the Advances in Neural Information Processing Systems (NeurIPS)*, 2016, pp. 4114–4122.
- [63] M. Li, W. Zuo, S. Gu, D. Zhao, and D. Zhang, "Learning convolutional networks for content-weighted image compression," in *Proceedings of the IEEE Conference on Computer Vision and Pattern Recognition (CVPR)*, 2018, pp. 3214–3223.
- [64] V. Nair and G. E. Hinton, "Rectified linear units improve restricted boltzmann machines," in *Proceedings of the International Conference on Machine Learning (ICML)*, 2010.
- [65] J. Zhang and B. Ghanem, "Ista-net: Interpretable optimization-inspired deep network for image compressive sensing," in *Proceedings of the IEEE Conference on Computer Vision and Pattern Recognition (CVPR)*, 2018, pp. 1828–1837.
- [66] E. Zisselman, A. Adler, and M. Elad, "Compressed learning for image classification: A deep neural network approach," in *Handbook of Numerical Analysis*, 2018, pp. 3–17.
- [67] O. Russakovsky, J. Deng, H. Su, J. Krause, S. Satheesh, S. Ma, Z. Huang, A. Karpathy, A. Khosla, M. Bernstein et al., "Imagenet large scale visual recognition challenge," *International Journal of Computer Vision*, vol. 115, pp. 211–252, 2015.
- [68] B. Zhou, H. Zhao, X. Puig, T. Xiao, S. Fidler, A. Barriuso, and A. Torralba, "Semantic understanding of scenes through the ade20k dataset," *International Journal of Computer Vision (IJCV)*, vol. 127, pp. 302–321, 2019.
- [69] R. Mottaghi, X. Chen, X. Liu, N.-G. Cho, S.-W. Lee, S. Fidler, R. Urtasun, and A. Yuille, "The role of context for object detection and semantic segmentation in the wild," in *Proceedings of the IEEE Conference on Computer Vision and Pattern Recognition (CVPR)*, 2014, pp. 891–898.
- [70] M. Cordts, M. Omran, S. Ramos, T. Rehfeld, M. Enzweiler, R. Benenson, U. Franke, S. Roth, and B. Schiele, "The cityscapes dataset for semantic urban scene understanding," in *Proceedings of the IEEE Conference on Computer Vision and Pattern Recognition (CVPR)*, 2016, pp. 3213–3223.
- [71] R. Wightman, "Pytorch image models," <https://github.com/rwightman/pytorch-image-models>, 2019.
- [72] K. He, X. Zhang, S. Ren, and J. Sun, "Deep residual learning for image recognition," in *Proceedings of the IEEE Conference on Computer Vision and Pattern Recognition (CVPR)*, 2016, pp. 770–778.
- [73] X. Chu, Z. Tian, Y. Wang, B. Zhang, H. Ren, X. Wei, H. Xia, and C. Shen, "Twins: Revisiting the design of spatial attention in vision transformers," in *Proceedings of the Advances in Neural Information Processing Systems (NeurIPS)*, 2021, pp. 9355–9366.
- [74] J. T. Springenberg, A. Dosovitskiy, T. Brox, and M. Riedmiller, "Striving for simplicity: The all convolutional net," *arXiv preprint arXiv:1412.6806*, 2014.
- [75] H. Zhao, J. Shi, X. Qi, X. Wang, and J. Jia, "Pyramid scene parsing network," in *Proceedings of the IEEE Conference on Computer Vision and Pattern Recognition (CVPR)*, 2017, pp. 2881–2890.
- [76] X. Li, H. Zhao, L. Han, Y. Tong, S. Tan, and K. Yang, "Gated fully fusion for semantic segmentation," in *Proceedings of the AAAI conference on artificial intelligence (AAAI)*, 2020, pp. 11 418–11 425.
- [77] J. He, Z. Deng, L. Zhou, Y. Wang, and Y. Qiao, "Adaptive pyramid context network for semantic segmentation," in *Proceedings of the IEEE Conference on Computer Vision and Pattern Recognition (CVPR)*, 2019, pp. 7519–7528.
- [78] Z. Huang, X. Wang, L. Huang, C. Huang, Y. Wei, and W. Liu, "Ccnnet: Criss-cross attention for semantic segmentation," in *Proceedings of the IEEE International Conference on Computer Vision (CVPR)*, 2019, pp. 603–612.
- [79] M. Contributors, "MMSegmentation: Openmmlab semantic segmentation toolbox and benchmark," <https://github.com/open-mmlab/mmssegmentation>, 2020.
- [80] Y. Koren, "Factorization meets the neighborhood: a multifaceted collaborative filtering model," in *Proceedings of the 14th ACM SIGKDD International Conference on Knowledge Discovery and Data Mining*, 2008, pp. 426–434.
- [81] J. Zhang, D. Zhao, C. Zhao, R. Xiong, S. Ma, and W. Gao, "Image compressive sensing recovery via collaborative sparsity," *IEEE Journal on Emerging and Selected Topics in Circuits and Systems*, vol. 2, pp. 380–391, 2012.
- [82] J. Zhang, D. Zhao, and W. Gao, "Group-based sparse representation for image restoration," *IEEE Transactions on Image Processing (TIP)*, vol. 23, pp. 3336–3351, 2014.
- [83] E. J. Candes, "The restricted isometry property and its implications for compressed sensing," *Comptes Rendus Mathématique*, vol. 346, no. 9–10, pp. 589–592, 2008.
- [84] P. G. Poličar, M. Stražar, and B. Zupan, "OpenTSNE: a modular python library for t-SNE dimensionality reduction and embedding," *BioRxiv*, p. 731877, 2019.



Chong Mou is currently pursuing the M.S. degree at the School of Electronic and Computer Engineering, Peking University Shenzhen Graduate School, Shenzhen, China. He received the B.S. degree at South China University of Technology, in 2020. His research interests include image denoising, feature attention, pattern recognition and deep learning.



Jian Zhang (M'14) received the B.S. degree from the Department of Mathematics, Harbin Institute of Technology (HIT), Harbin, China, in 2007, and received his M.Eng. and Ph.D. degrees from the School of Computer Science and Technology, HIT, in 2009 and 2014, respectively. From 2014 to 2018, he worked as a post-doctoral researcher at Peking University (PKU), Hong Kong University of Science and Technology (HKUST), and King Abdullah University of Science and Technology (KAUST).

Currently, he is an Assistant Professor with the School of Electronic and Computer Engineering, Peking University Shenzhen Graduate School, Shenzhen, China. His research interests include intelligent multimedia processing, deep learning and optimization. He has published over 90 technical articles in refereed international journals and proceedings. He received the Best Paper Award at the 2011 IEEE Visual Communications and Image Processing (VCIP) and was a co-recipient of the Best Paper Award of 2018 IEEE MultiMedia.